

# Cell non-autonomy amplifies disruption of neurulation by mosaic Vangl2 deletion

**Gabriel Galea** (✉ [g.galea@ucl.ac.uk](mailto:g.galea@ucl.ac.uk))

UCL GOS Institute of Child Health <https://orcid.org/0000-0003-2515-1342>

**Eirini Maniou**

UCL GOS Institute of Child Health

**Abigail R Marshall**

UCL GOS Institute of Child Health

**Nicholas DE Greene**

UCL GOS Institute of Child Health

**Andrew J Copp**

UCL GOS Institute of Child Health

---

## Research Article

**Keywords:** Neural tube, spina bifida, mosaicism, apical constriction, Vangl2

**Posted Date:** September 9th, 2020

**DOI:** <https://doi.org/10.21203/rs.3.rs-73706/v1>

**License:**  This work is licensed under a Creative Commons Attribution 4.0 International License.

[Read Full License](#)

---

**Version of Record:** A version of this preprint was published at Nature Communications on September 9th, 2020. See the published version at <https://doi.org/10.1038/s41467-021-21372-4>.

# Abstract

Post-zygotic mutations that generate tissue mosaicism are increasingly associated with severe congenital defects, including those arising from failed neural tube closure. We observed that elevation of the neural folds during mouse spinal neurulation is vulnerable to deletion of the planar cell polarity core component Van Gogh-like (Vangl)2 in as few as 16% of neuroepithelial cells. Vangl2-deleted cells are typically dispersed throughout the neuroepithelium, and each non-autonomously prevents apical constriction by an average of five Vangl2-replete neighbours. This inhibition of apical constriction involves reduced myosin-II recruitment to neighbour cell borders and shortening of basally-extending microtubule tails, which are known to facilitate apical constriction. Vangl2-deleted cells themselves continue to apically constrict and preferentially recruit myosin-II to their apical cell cortex rather than to apical cap sarcomere-like organisations. Such non-autonomous effects can explain how post-zygotic mutations affecting a minority of cells can cause catastrophic failure of morphogenesis leading to clinically important birth defects.

## Introduction

Neural tube (NT) defects such as spina bifida continue to affect an average of 1:1,000 pregnancies globally, with higher disease burden in developing countries<sup>1</sup>. They arise due to failure of NT closure in the early embryo<sup>2</sup>. Mouse models faithfully recapitulate these conditions and have historically led to the identification of diagnostic and preventative strategies, as well as identifying genes and pathways required for NT closure<sup>3-5</sup>. Key genes include members of the Wnt/planar cell polarity (PCP) pathway and enzymes of folate metabolism<sup>6</sup>, with the latter already a clinical target for primary prevention. Homozygous mutation of core PCP components reproducibly produces the most severe form of NT defect, craniorachischisis, in which much of the brain and all of the spinal cord remain open<sup>2</sup>. Mutations in core PCP components have been identified in human foetuses with craniorachischisis<sup>7</sup> and in individuals with NT defects such as spina bifida<sup>8,9</sup>. Nonetheless, most affected families do not receive an interpretable genetic diagnosis. One possible explanation is that disease-causing mutations may arise during post-zygotic embryonic development, rather than in the germ line, producing mosaicism that is not readily detectable with conventional genetic diagnostic methods<sup>10,11</sup>. Indeed, post-zygotic mutations in PCP components have recently been implicated in human spina bifida<sup>10</sup>.

Mouse neurulation starts with narrowing and elongation of the relatively flat neural plate through PCP-dependant convergent extension. Neural folds subsequently elevate at the neural plate edges and meet at the embryonic dorsal midline, “zippering” to propagate closure along the length of the embryo<sup>2</sup>. Caudal to the initiation site, Closure 1, the region of open spinal neural folds (termed the posterior neuropore, PNP) undergoes closure through a fundamentally biomechanical process, requiring force-generating cellular behaviours such as apical constriction to elevate and appose the neural folds<sup>12,13</sup>. Analysis of Vangl2’s roles in spinal NT closure is hindered by the fact that its homozygous deletion precludes the earlier step of closure initiation<sup>14,15</sup>. Heterozygous Vangl2 mutant mice close their PNP successfully in most cases,

although a very small percentage develop open spina bifida<sup>5</sup>. In keeping with this, heterozygous PCP gene mutations have been associated with spina bifida in humans<sup>9,16</sup>, although the mechanisms linking such genetic findings with failed NT closure are unclear.

We recently reported that targeted deletion of *Vangl2* by *Grhl3<sup>Cre</sup>* in a proportion of neuroepithelial cells and throughout the surface ectoderm causes distal spina bifida<sup>13</sup>. In that model, spina bifida was preceded by failure of neural fold elevation and biomechanical disruption of closure. The uninducible, multi-lineage recombination of *Grhl3<sup>Cre</sup>* precluded attribution of *Vangl2*'s primary role to either the neuroepithelium or surface ectoderm. In other epithelia, PCP complexes comprise asymmetric trans-membrane components between neighbouring cells, with *Vangl* and *frizzled* located on opposing surfaces<sup>17</sup>. Core components are preferentially oriented on either rostral/proximal or caudal/distal cell membranes, such that tissue polarity emerges non-cell autonomously. Consequently, mislocalisation of PCP components in individual mutant cells necessarily prevents their neighbours from correctly localising the opposing complex components<sup>18-20</sup>. Protein-level planar-polarised orientation of *Vangl2* is not apparent in the late PNP of the mouse embryo, where pseudostratified neuroepithelial cells have complex apical shapes often without predictably oriented borders<sup>13,21</sup>. Nonetheless, planar-polarised properties do emerge in this complex epithelium, including preferential arrangement of cell apices and supra-cellular actomyosin profiles in a mediolateral orientation<sup>13,21</sup>.

Actomyosin reorganisation is a well-documented outcome of *Vangl*/PCP signalling<sup>22-25</sup>. Pulsed recruitment of actomyosin to the apical surface is necessary for epithelial apical constriction<sup>26,27</sup>. Mechanisms of apical constriction described in different cell types require radial apical sarcomere-like organisations or cortical actomyosin driving sequential junctional shrinkage<sup>28</sup>.

Both the spatial and temporal pattern of actomyosin recruitment to epithelial apical surfaces is regulated by PCP signalling. In *Xenopus*, knockdown of PCP components accelerates pulses of myosin recruitment to the apical cell cortex<sup>29</sup>. Shuttling of actomyosin contractility regulators towards the cell's apex is facilitated by microtubules in many different epithelia and stabilised microtubule bundles correlate with the onset of apical constriction during various morphogenetic events<sup>30-34</sup>. However, microtubules may also oppose apical constriction. Their polymerisation continuously pushes against cell junctions, curving under compressive forces from actomyosin-generated constriction<sup>35</sup>. Knockdown of *Vangl2* in mammalian Sertoli cells causes reorganisation of microtubules from long bundles into short, disorganised fragments<sup>36</sup>, and in oligodendroglial cells *Vangl2* increases microtubule density<sup>37</sup>. Thus both the microtubule and actomyosin cytoskeletons are *Vangl2* targets and contribute to apical constriction.

Neuroepithelial apical constriction has been documented in the mouse by ourselves and others<sup>12,21,38,39</sup>. The neuroepithelium has a predominantly apical localisation of F-actin and non-muscle myosin-II<sup>40,41</sup>. Pharmacological inhibition of myosin activation reduces apical neuroepithelial mechanical tension and causes PNP widening<sup>21</sup>. The molecular regulation of apical constriction has been extensively studied in

non-mammalian vertebrates, demonstrating cell-autonomous basolateral-to-apical shuttling of myosin onto an apical F-actin network<sup>23,29,42</sup>. Mouse embryos have been less amenable to sub-cellular resolution live imaging of neurulation due to their fragility, awkward 3D shape and movement artefact partly caused by their heartbeat, which is a desirable indicator of embryo viability. Previous live imaging of early mouse embryos, prior to formation of the PNP, demonstrated that global mutation of *Vangl2* reduces neural plate apical neighbour exchange during convergent extension movements without altering basal protrusive activity<sup>43</sup>. We have recently optimised mouse whole-embryo static culture for live imaging of later-stage embryos to allow sub-cellular visualisation of “zippering”<sup>44</sup>.

Here we provide mechanistic evidence that mosaicism for somatic mutations in PCP components, even with only a small minority of mutant neuroepithelial cells, is indeed sufficient to cause NT defects. We explore the hypothesis that non-cell autonomous effects amplify the morphogenetic disruption caused by mosaic mutations. We find that *Vangl2*-deleted cells prevent multiple neighbours from recruiting myosin-II to their cell cortex, thereby diminishing the apical constriction of a majority of neuroepithelial cells. Remarkably, *Vangl2*-deleted cells themselves continue to constrict apically. Nevertheless, the amplifying effect of the non- autonomous anti-morphogenetic influence of mosaic *Vangl2*-deletion leads to reduction in apical neuroepithelial mechanical tension and failure of neural fold elevation, causing spina bifida.

## Results

### Mosaic neuroepithelial *Vangl2* deletion counteracts posterior neuropore closure

Induced deletion of *Vangl2* in a minority of neuroepithelial cells is sufficient to stall PNP closure, as we found previously when *Vangl2* deletion in a small proportion of cells using the constitutive *Grhl3<sup>Cre</sup>* produced distal spina bifida<sup>13</sup>. *Grhl3<sup>Cre</sup>* recombines conditional alleles ubiquitously in the surface ectoderm and mosaically in the neuroepithelium (Supplementary Figure 1A), precluding attribution of *Vangl2* requirement to either tissue. To our knowledge, no currently available constitutive Cre drivers selectively yet persistently lineage trace the ventral PNP neuroepithelium. Tamoxifen-inducible CreERT2 drivers are limited because early tamoxifen administration by intra-peritoneal injection prevents embryo implantation and is teratogenic<sup>45</sup>. We recently validated an oral tamoxifen administration protocol which robustly activates embryonic CreERT2 without impeding NT closure<sup>46</sup>. Using this method to induce *Sox2<sup>CreERT2</sup>* led to extensive lineage tracing of neuroepithelial cells in the closed NT, but only to a very limited extent in the open PNP (Supplementary Figure 1B)<sup>47</sup>. In contrast, the neuromesodermal progenitor marker *Nkx1.2<sup>CreERT2</sup>* lineage traces cells in both ventral PNP and closed NT<sup>48</sup> (Figure 1A-C). Moreover, it produces mosaic neuroepithelial recombination similarly to *Grhl3<sup>Cre</sup>* (Supplementary Figure 1A, C).

In *Nkx1.2<sup>CreERT2/+</sup>; Vangl2<sup>Fl/-</sup>; Rosa26<sup>mTmG/+</sup>* embryos (henceforth called Cre;Fl/-), CreERT2- induced EGFP reporter expression identifies cells in which *Vangl2* has been deleted, 24 h after tamoxifen treatment (Figure 1D,E). Relative *Vangl2* reduction is significantly greater when one allele is pre-deleted in Cre;Fl/-

embryos compared with Cre;Fl/Fl (Figure 1D). This produces a patchy, mosaic pattern of Vangl2 deletion in the neuroepithelium (Figure 1F).

The PNP fails to close, producing pre-spina bifida lesions, in 54% (7/13) of Cre;Fl/- embryos at E10.5 compared with 0% (0/23, Fisher's exact test  $p < 0.001$ ) of Cre;Fl/Fl embryos. Cre;Fl/Fl embryos occasionally develop dorsally flexed tails suggestive of delayed PNP closure (Supplementary Figure 2A). In this study, Cre-negative littermate embryos were used as controls for the Cre;Fl/Fl and Cre;Fl/- genotypes. Vangl2-deleted cells, lineage traced with EGFP, are more abundant in the dorsal closed NT of Cre;Fl/- embryos with pre-spina bifida lesions than those which achieve PNP closure (Figure 1G, Supplementary Figure 2C). Even so, there is substantial overlap between these groups and embryos which fail to close their PNPs only lose Vangl2 in around 16% of neuroepithelial cells (Supplementary Figure 2C).

Pre-spina bifida lesions reflect a pathological state which is difficult to compare to control embryos with physiological, closed NT. Morphometric analyses were therefore performed at earlier developmental stages to identify the first quantifiable phenotype before failure of PNP closure. Dorsolateral and medial hinge points do not differ overtly between the PNPs of Cre;Fl/- and control embryos (Figure 1H), whereas PNP length is significantly longer in Cre;Fl/- embryos than in controls at late stages of closure (Figure 1I). Preceding this, the neural folds are less elevated in Cre;Fl/- embryos than in controls (Figure 1J,K). Thus, the first morphometrically quantifiable tissue-level consequence of mosaic Vangl2 deletion is failure of neural fold elevation. Neither PNP length (Supplementary Figure 2B) nor neural fold elevation (Figure 1K) were significantly different between Cre;Fl/Fl embryos and Cre-negative controls, and there was no significant difference in neuroepithelial thickness between genotypes (Figure 1L).

At the cellular level, mediolateral orientation of cell apical surfaces is a readily quantifiable planar-polarised phenotype in the mouse PNP neuroepithelium<sup>13</sup>. Cells in control embryos, as well as both EGFP and tdTom cells in Cre;Fl/Fl embryos had preferentially mediolaterally- oriented apical surfaces (median orientation 52-53°, Figure 2A-C). In contrast, neither Vangl2- deleted (EGFP) nor Vangl2-replete (tdTom) cells showed preferential mediolateral orientation in Cre;Fl/- embryos (median orientation 42° each, Figure 2B). The proportions of deleted and replete cells in each orientation bracket were significantly different from control embryos (Figure 2B). Apical orientations of Vangl2-deleted and -replete cells did not differ significantly from each other, suggesting non-autonomous disruption of apical planar polarity. However, median apical cellular areas were smaller in Vangl2-deleted cells than in Vangl2-replete cells in the same Cre;Fl/- embryos, and smaller than cells in control embryos (Figure 2D). Vangl2 deletion did not alter neuroepithelial proliferation (Supplementary Figure 2D-E).

## Mosaic Vangl2 deletion diminishes neuroepithelial apical constriction

In both mouse and chick embryos, neural fold elevation requires apical tension generated by actomyosin-dependent apical constriction<sup>21,25</sup> and variable apical areas in Cre;Fl/- embryos suggest differential constriction within the mosaic neuroepithelium. Cellular mechanical tension is commonly inferred from recoil of cell borders immediately following laser ablation. We previously demonstrated that annular laser ablations in the apical neuroepithelium produce actomyosin-dependant, rapid initial shrinkage of the cluster of cells within the annulus as they are untethered from the surrounding tissue<sup>21</sup>. Here, the reduction in apical area of cells or cell clusters following ablation will be referred to as “retraction” to differentiate it from spontaneous apical “constriction” during live imaging. Apical retraction is smaller in some neuroepithelial cells in Cre;Fl/- embryos (Figure 3A-C), but not in Cre;Fl/Fl (Supplementary Figure 3A), compared with controls.

In Cre;Fl/- embryos, the reduction in apical retraction is limited to cell clusters which include Vangl2-deleted cells. Selective annular ablations which do not include Vangl2-deleted cells in Cre;Fl/- embryos produce equivalent retractions to control embryos (Figure 3C). This shows apical tension is diminished locally in association with the deleted cells.

To test whether the local diminution of neuroepithelial apical retraction around Vangl2-deleted cells occurs cell autonomously, apical areas of Vangl2-deleted EGFP<sup>+</sup> cells were analysed separately from their Vangl2-replete tdTom<sup>+</sup> neighbours. Whereas Vangl2-deleted cells were found to retract similarly to cells in control embryos, their Vangl2-replete neighbours retracted less (Figure 3E-G). Both EGFP<sup>+</sup> cells and tdTom<sup>+</sup> neighbours retracted similarly to controls in Cre;Fl/Fl embryos (Supplementary Figure 3B). Thus, the diminution of apical retraction following mosaic Vangl2 deletion is non-cell autonomous: Vangl2-replete neighbours of Vangl2-deleted cells fail to undergo apical retraction, whereas the Vangl2-deleted cells themselves continue to retract.

Potential explanations for differential retraction following laser ablation include changes in cell adhesion, material properties, or actomyosin-dependent constriction. Vangl2-deleted cells and their neighbours continue to assemble adherens junctions labelled with N-cadherin and active  $\beta$ -catenin, as well as tight junctions labelled with ZO-1 and an apical F-actin cortex (Supplementary Figure 4A-B). These findings suggest that neither neuroepithelial cell-cell adhesion nor cortical actin differences explain differential apical retraction differences. We therefore sought to directly assess apical constriction through visualisation in live-imaged embryos. The length of live-imaged sequences was limited by substantial changes in tissue morphology as the PNP continued to narrow (Supplementary Figure 5A) and time constraints of imaging at least one control and one comparable Cre;Fl/- embryo from each litter, while avoiding prolonged culture. Live-imaged sequences were therefore limited to 20 minutes. Over this time, neuroepithelial cells were found to vary their apical surfaces in an asynchronous, frequently pulsatile manner characteristic of apical constriction in other cell types (Supplementary Figure 5B-D). Individual cells could be in constriction or dilation phases at the start of imaging. In order to rationalise the data, the apical sizes of individual cells were temporally aligned by their largest observed apical area. This produced averaged traces of dilation followed by constriction (Supplementary Figure 5B-D). A pilot study

analysing a wild-type embryo showed that 24 cells need to be analysed to detect a 20% difference in apical area reduction ( $p = 0.05$ , power = 0.8).

Vangl2-deleted cells in Cre;Fl/- embryos dilate faster than cells in control embryos, but subsequently constrict at a similar rate (Figure 4A-C). This pattern could be explained by either a change in constriction frequency or magnitude, but we cannot discriminate between these with the available data (Supplementary Figure 5E). In contrast, Vangl2-replete neighbours of Vangl2- deleted cells dilate similarly to controls, but then fail to constrict (Figure 4D). Vangl2-replete cells which do not contact Vangl2-deleted cells in Cre;Fl/- embryos (“Distant” cells in Figure 4D) dilate and constrict similarly to cells in control embryos. These findings corroborate the laser ablation analyses by implicating non-autonomous failure of apical constriction in Vangl2- replete “neighbour” cells, which leads to diminution of overall neuroepithelial apical tension.

Three subgroups of cells were defined for further analysis: 1) Vangl2<sup>-</sup>/EGFP<sup>+</sup> cells which constrict, 2) Vangl2<sup>+</sup>/EGFP<sup>-</sup> “neighbouring” cells which do not constrict and, 3) Vangl2<sup>+</sup>/EGFP<sup>-</sup> “distant” cells which do constrict (Figure 4d).

## Mosaic Vangl2 deletion alters the actomyosin and microtubule cytoskeletons

Cytoskeletal regulation by Vangl2/PCP signalling is well established in other contexts, and both actomyosin and microtubule changes may underlie differential apical constriction in the neuroepithelium following mosaic Vangl2 deletion<sup>22-24,36,49,50</sup>. Neuroepithelial cells assemble apical phosphorylated, active non-muscle myosin light chain-II around their cell cortex (Figure 5A). In addition, phospho-myosin light chain (pMLC)-II decorates the apical cap of individual neuroepithelial cells (Figure 5A). This pattern is accentuated when total myosin heavy chain (MHC)-IIb is visualised, producing marked differences in localisation to the cell cortex, with or without staining on apical caps (Figure 5B). The same pattern is observed with a second commercial anti-MHC-IIb antibody (Supplementary Figure 6A).

The effect of mosaic Vangl2 deletion on both cortical and apical cap MHC-IIb was assessed sequentially. Cortical MHC-IIb staining between neuroepithelial cells with varying contractility behaviour was defined as above. MHC-IIb staining visualised on cell borders is the average between adjacent cells: 1) “EGFP/neighbour” borders are between a contractile and a non-contractile cell, 2) “neighbour/neighbour” borders are between two non-contractile cells, and 3) “distant/distant” borders are between two contractile cells. Average MHC-IIb staining intensity was found to be highest along the most contractile distant/distant borders of Cre;Fl/- embryos, whereas EGFP/neighbour and neighbour/neighbour borders had significantly lower intensity that did not differ between them (Figure 5C).

MHC-IIb is enriched on the apical cap of approximately half of PNP neuroepithelial cells in wild-type embryos (Figure 5D-E). Apical cap MHC-IIb forms a sarcomere-like pattern of punctate staining or linear

arrangements resembling stress fibres (Figure 5D “cap”). However, Vangl2-deleted cells show primarily cortical, rather than apical cap MHC-IIb staining (Figure 5E). This effect is cell-autonomous as neither neighbouring nor distant EGFP<sup>+</sup>/Vangl2<sup>+</sup> cells in Cre;Fl/- embryos are different from controls (Figure 5E).

Similar apical sarcomere-like arrangements have been described in insect cells, and are enhanced in mammalian cells with diminished microtubule turnover<sup>51</sup>. Vangl2 deletion alters microtubule organisation in other mammalian cells<sup>36,37</sup>. Non-mitotic PNP neuroepithelial cells were found to assemble microtubules in two predominant patterns: apically-enriched radiating fibres versus apicobasally-elongated “tails” (Figure 5F). Both apical pools and the elongated tails stain positively for the stable microtubule marker acetylated tubulin (Supplementary Figure 6B). Both of these microtubule arrangements influence apical constriction in other contexts: apical networks counteract, whereas apicobasal tails promote constriction<sup>33-35,52</sup>.

Apical radiating microtubule fibres were mainly seen in neuroepithelial cells with apical cap myosin, whereas elongated tails were found to be associated with a primarily cortical myosin distribution (Figure 5F). The small proportion of neuroepithelial cells in mitosis at any one time have a tubulin network which is apical to and distinct from the centrosomal network (Supplementary Figure 6C). Both these microtubule patterns are preserved in neuroepithelia with mosaic Vangl2 deletion, but the length of microtubule tails was found to be shorter in Cre;Fl/- embryos than in wild-type littermates (Figure 5G). This effect appears non-autonomous as Vangl2-deleted cells have longer tails than their neighbours (Figure 5H-I). Conversely, Vangl2- deleted cells have less abundant apical microtubule networks than their neighbours (Figure 5J,K).

Thus, Vangl2-deleted cells preferentially localise myosin to the contractile cell cortex in a cell-autonomous manner, while both autonomously and non-autonomously altering microtubule organisation in a pattern expected to favour their constriction (Figure 5L).

## Non-autonomy amplifies mosaic Vangl2 deletion

Having demonstrated non-autonomous suppression of apical constriction by Vangl2-deleted cells, we sought to quantify the potential for effect amplification as a result of each deleted cell inhibiting multiple neighbours. Lewis' law predicts that the apical area of epithelial cells should correlate linearly with the number of cells they neighbour, and that the average cell should have six apical neighbours<sup>53,54</sup>. In agreement with this law, Vangl2-deleted cells have 5.7 total neighbours on average, of which 5.3 are Vangl2-replete (Figure 6A-B). The proportion of Vangl2-replete cells neighbouring a Vangl2-deleted cell is greater in embryos with more recombined cells within the range of recombination achievable with *Nkx1.2<sup>CreERT2</sup>* (Figure 6C). However, cells share neighbours, so the number of unique neighbours per Vangl2-deleted cell decreases as the proportion of deleted cells increases (neighbours/deleted cell shown in Figure 6D). In other words, as more cells lose Vangl2 they each have fewer unique neighbours. Thus,

neighbour-sharing limits amplification of effect size through non-autonomy and individual Vangl2-deleted cells have the greatest impact in embryos with low levels of recombination.

To test this, we investigated correlations between the proportion of Vangl2-deleted cells versus neural fold eversion, the earliest phenotype detected in Cre;Fl/- embryos. The proportion of Vangl2-deleted neuroepithelial cells does not correlate with magnitude of neural fold eversion (Figure 6E). However, the proportion of Vangl2<sup>+</sup>EGFP<sup>-</sup> neighbour cells is significantly correlated with neural fold eversion (Figure 6F). This supports a model in which non-autonomous inhibition of neighbour cells' apical constriction underlies failure of PNP closure following mosaic Vangl2 deletion.

## Discussion

Post-zygotic somatic mutations are pervasive<sup>55,56</sup>. Human foetal forebrain neural progenitors accumulate 8.6 new genomic variants per cell division and each harbours up to 12 non-benign variants<sup>57</sup>. The importance of somatic mosaicism is clinically established in dermatology, causing both malignant transformation and benign phenotypes<sup>58</sup>. One such example is epidermal nevus syndrome, which affects 1-3:1,000 births<sup>59</sup>. This prevalence is comparable to that of NT defects. Post-zygotic mutations have been implicated in various congenital malformations<sup>60,61</sup> and mutations in PCP components have specifically been identified in patients with NT defects<sup>10</sup>. Here we demonstrate, in a mammal, that these mutations only need to disrupt PCP in a small percentage of neuroepithelial cells, around 16%, to cause spina bifida.

Presumptive spinal cord neuroepithelial cells are thought to primarily derive from neuromesodermal progenitors which persist throughout neurulation<sup>62,63</sup>. Thus, *de novo* mutations in this population would be propagated to their daughter cells throughout PNP closure. We took advantage of this property in the current study to persistently delete Vangl2 in a variable proportion of neuroepithelial cells using *Nkx1.2<sup>CreERT2</sup>*. Resulting deletion of Vangl2 occurs relatively late in neurulation, after the convergent extension movements which initiate NT closure at E8-8.5. This Cre-driver does not itself impair NT closure even when homozygous<sup>48</sup>, nor when used to delete *Rac1*<sup>64</sup>. In the current study, a single administration of tamoxifen only predictably deleted Vangl2 when one allele was pre-deleted. Single administration was critical to ensure predictable deletion dynamics such that EGFP lineage tracing could be used to identify Vangl2-deleted cells. Pre-deletion of a Vangl2 allele followed by Cre-mediated recombination represents two genetic hits. It is less likely that two somatic mutations would occur in the same gene, in the same cell, spontaneously. However, double heterozygous mutations of different PCP components is sufficient to cause NT defects<sup>65</sup> and di-genic variants in PCP components are readily documented in human patients<sup>16</sup>.

Human mutations in core PCP genes disrupt this pathway when engineered into *Drosophila*<sup>66</sup>. Mammalian embryonic tissues achieve planar polarity through ligand gradient-sensing, as in the case of Fat/Dachsous PCP, or through non-autonomous propagation of directionality through asymmetrical

complex organisation characteristic of the 'core' PCP pathway studied here<sup>17,67</sup>. In *Drosophila* epithelia, asymmetrical PCP localisation emerges gradually from seemingly-homogeneous initial distributions<sup>68,69</sup>. This may also happen in mammals, as for example indicated by the finding of more apparent Vangl2 planar polarity at later stages of oviduct maturation in mice<sup>70</sup>. Symmetry-breaking of membrane complexes may be induced by mutual repulsion between core components, directional trans-endocytosis of Vangl2 between adjacent cells, or extrinsic cues such as mechanical tension<sup>17,67,68</sup>. Immunolocalisation of mammalian PCP components is notoriously limited by the unavailability of adequate antibodies, although the knockout-validated 2G4 anti-Vangl2 antibody<sup>71</sup> used here allows robust detection of Vangl2 in the mouse PNP. Vangl1 is not widely expressed in the mouse PNP neuroepithelium<sup>72</sup>. This makes Vangl2 a particularly valuable target to explore the functions of PCP signalling during PNP closure. Ubiquitous Vangl2 deletion causes failure of convergent extension migration at the onset of neurulation<sup>14</sup> whereas, after the PNP forms, neuroepithelial cells migrate laterally and dorsally to form the dorsolateral hinge points<sup>73</sup>. Vangl2 appears to control convergent extension cell-autonomously. In chimeric embryos containing Vangl2-mutant cells, the wild-type cells self-segregate during early convergent extension of the neural plate<sup>14</sup>. This contrasts with non-autonomous control of apical constriction described here.

While the role of PCP signalling in polarised junction shrinkage which underlies convergent extension is well established, its role in regulating apical constriction is incompletely understood. Substantial progress has been made by studying chick neurulation, where knockdown of PCP core components results in larger neuroepithelial apical sizes and failure of neural plate dorsal bending consistent with failed apical constriction<sup>25</sup>, as seen in mice in this study. The molecular mechanisms underlying this phenotype involve dishevelled-dependant recruitment of Rho-kinase (Rock) and the F-actin polymerising protein dishevelled-associated activator of morphogenesis (Daam1)<sup>25</sup>. Vangl2 may suppress this contractile machinery because it suppresses dishevelled/Daam1 interaction<sup>74</sup>, potentially explaining why Vangl2-deleted cells apically constrict more than their neighbours. Previous mouse studies suggest aspects of this pathway are conserved in mammals: pharmacological inhibition of Rock similarly stops apical constriction in mouse embryos, and although Daam1 homozygous deletion does not stop NT closure it interacts genetically with heterozygous Vangl2 mutation to cause spina bifida<sup>75</sup>. However, there are important species differences in this pathway between chick and mouse embryos. Whereas pharmacological Rock inhibition very dramatically reduces neuroepithelial F-actin intensity in chick embryos<sup>25,76</sup>, its inhibition with the same compound expands the region of F-actin localisation due to an increase in F- versus G-actin proportion in mouse embryos<sup>21,40</sup>. Additionally, whereas the adherens junctions in the anterior chick neuroepithelium are primarily composed of high-affinity E-cadherin<sup>25,77</sup>, the mouse PNP neuroepithelium exclusively expresses lower-affinity N-cadherin protein<sup>78,79</sup>. Here we show that these adherens junction complexes remain apparent in both Vangl2-deleted cells and their neighbours.

Adherens junctions physically couple the contractile actomyosin cytoskeleton between cells, allowing force transmission across epithelia. Two pools of myosin generate apical constriction forces transmitted through these junctions: circumferential contractile networks around the cell cortex and sarcomere-like medio-apical networks<sup>28</sup>. Previous studies of myosin activation in the apical neuroepithelium have identified cortical networks in mouse, chick and *Xenopus*.

Phosphorylated, “active” myosin-II is primarily localised to these cell borders. A large body of work in *Xenopus* demonstrates that the apical determinant Par3 physically associates with PCP components to localise them at the apical surface<sup>80</sup> where they reside preferentially at contractile cell-cell junctions<sup>81</sup>. Resulting apical constriction of neuroepithelial cells requires the endosomal trafficking protein Rab11<sup>82</sup>, whose apical translocation is Vangl2-dependant in *Xenopus* blastopore lip cells<sup>23</sup>. While it has not yet been possible to determine whether these molecular interactions are conserved in mammals, here we demonstrate that the presence of Vangl2 is required for neighbouring cells to recruit myosin-II to their cortex.

In addition to its predominantly cortical localisation, super-resolution imaging also revealed active myosin on the mouse neuroepithelium apical cap. Visualisation of apical cap myosin was substantially improved when total myosin-IIb was visualised. We propose this difference is likely due to simple stoichiometry: the phosphorylated form of the small regulatory light chain presents a far less substantial target for visualisation than the long heavy chain. Alternative explanations may include differential turnover of apical cap myosin, or F-actin cross-linking roles of myosin-II independently of its regulatory light chain-dependant motor function<sup>83,84</sup>.

Irrespective, the co-occurrence of apical myosin and dense apical microtubules in interphase cells is striking. The actomyosin and microtubule cytoskeletons are physically linked and myosin contractility deforms the microtubule network<sup>85,86</sup>. It is therefore intriguing to speculate that apical cap myosin contractility may have a role in partitioning or redistribution of apical microtubule cargoes beyond its purported role in apical constriction. Stopping myosin activation, through expression of dominant negative Rock or constitutively active myosin phosphatase, prevents anterior localisation of Vangl2 in the apical surface of the *Xenopus* neuroepithelium<sup>24</sup>. Apical localisation of PCP components occurs through trafficking in vesicles along apicobasally- oriented microtubules in the zebrafish neuroepithelium<sup>50</sup>.

Apicobasally-oriented non-centrosomal microtubule tails have been extensively documented in the *Xenopus* neuroepithelium<sup>87-89</sup>. The consensus that they biomechanically contribute to NT closure in that model is consistent with our findings. Here we show that Vangl2 deletion non- autonomously shortens microtubule tails in the mouse neuroepithelium, placing Vangl2 upstream of microtubule organisation. However, whereas the primary function of microtubule tails in the bi-layered *Xenopus* neuroepithelium is believed to be cell elongation<sup>90</sup>, shortened tails in the pseudostratified epithelium of Cre;Fl/- embryos were not associated with apical-basal shortening. Our findings are also in contrast to previous studies which implicate microtubule polymerisation in the establishment and maintenance of PCP component

polarisation<sup>50,91</sup>. Molecular mechanisms underlying this seemingly bi-directional interaction are a matter for future work, but our findings reveal a dynamic interplay between PCP, microtubules and actomyosin in the mammalian neuroepithelium. It has been suggested that promotion of apical constriction is one of the beneficial consequences of folate which may contribute to its ability to prevent a proportion of human NT defects<sup>92,93</sup>. These interactions may therefore be specifically disrupted in patients with mosaic PCP mutations and may identify more widely-applicable therapeutic targets.

Patients with non-syndromic NT defects rarely receive a genetic diagnosis relevant to prevention or genetic counselling. Our findings may begin to explain this short-fall. Mutations in neuromesodermal progenitor cells which affect only a small proportion of neuroepithelial cells would not be detectable with diagnostic genotyping methods. These mutations may be predisposed to by agents known to decrease genomic stability and increase NT defect risk, including pollutants<sup>94-96</sup>, folate deficiency<sup>97,98</sup>, and diabetes<sup>99-102</sup>. Our findings provide a new framework to understand the consequences of mosaic mutations on congenital structural malformations.

## Methods

### *Animal procedures*

Studies were performed under the UK Animals (Scientific Procedures) Act 1986 and the Medical Research Council's Responsibility in the Use of Animals for Medical Research (1993). Mice were time-mated overnight and the morning a copulation plug was identified was considered E0.5. Heterozygous *Grhl3<sup>Cre/+</sup>*, *Nkx1.2<sup>CreERT2</sup>*, *Sox2<sup>CreERT2</sup>* and *Vangl2<sup>Fl/Fl</sup>*, *Rosa26<sup>mTmG</sup>* mice were as previously described<sup>103,104</sup> and were maintained on a C57BL/6 background. To generate parent stock, *Nkx1.2<sup>CreERT2/+</sup>* males were mated with *Vangl2<sup>Fl/-</sup>* females to generate *Nkx1.2<sup>CreERT2/+</sup>Vangl2<sup>Fl/-</sup>* studs, which were morphologically normal. From 8 weeks of age, *Nkx1.2<sup>CreERT2/+</sup>Vangl2<sup>Fl/-</sup>* studs were bred with *Vangl2<sup>Fl/Fl</sup>Rosa26<sup>mTmG/mTmG</sup>* females to generate embryos with the desired genotypes. Tamoxifen (10 mg/mouse) was administered at 8:00 a.m. on E8 as previously validated<sup>46</sup>.

Embryos were harvested around E9-10.5 as previously described<sup>105</sup> and rinsed in PBS prior to fixation in 4% paraformaldehyde, pH 7.4. For tubulin staining, embryos were dissected, washed and fixed in solutions pre-warmed to 37°C. Yolk sacs were collected from each embryo and genotyping was performed as previously reported<sup>64</sup>.

### *Whole mount staining*

All images are representative of observations in at least three embryos from independent litters. Primary antibodies were: rabbit anti-Vangl2 (Millipore clone 2G4, as previously validated<sup>71</sup>, 1:100 dilution), rabbit anti-MHCIIb (BioLegend PRB-445 and Abcam clone 3H2, 1:200), rabbit anti-Ser19 pMLCII (Cell Signalling Technology #3671, 1:100), rabbit anti-K40 acetylated  $\alpha$ -tubulin (Abcam EPR16772, 1:200), mouse anti- $\beta$ -tubulin (Insight Biotechnology clone AT5B2, 1:200), mouse anti- $\beta$ -catenin (Santa Cruz Biotechnology,

clone E-5, 1:100), mouse anti-N-cadherin (Cell Signalling Technology clone 13A9, 1:150), rabbit anti-Zo-1 (Thermo Scientific clone 40-2200, 1:100) and chicken anti-GFP (Abcam ab13970, 1:300). Alexa Fluor™ 405, 488, 568 and 647-conjugated secondary antibodies and phalloidin were from Thermo Scientific.

EGFP was typically detected using endogenous fluorescence, but this was quenched when antigen retrieval was required.

Paraformaldehyde-fixed embryos were permeabilised in PBS with 0.1% Triton X-100 (PBT) for 1 hr at room temperature, blocked overnight in a 5% BSA/PBT at 4°C and incubated overnight in a 1:150 dilution of primary antibody in blocking solution at 4°C. Embryos were then washed 3 x 1 hr at room temperature in blocking solution, incubated for 2 hrs at room temperature in 1:300 dilution of Alexa Fluor®-conjugated secondary antibodies. Excess secondary antibody was removed by washing for 1 hr in blocking solution and a further 2 x 1 hr in PBT at room temperature. Visualization of pMLC-II and N-Cadherin required antigen retrieval. This was performed by pre-incubating embryos in 10 mM sodium citrate acid, 0.05% Tween 20, pH 6.0 for 30 min at room temperature to ensure penetration throughout the embryo, replacing the sodium citrate solution and incubating the embryo at 95°C for 20 minutes, then cooling at room temperature for 30 minutes. In some cases, mild cross-reactivity of the anti-chick secondary was observed, producing faint additional signal in the EGFP track which did not impede identification of EGFP+ cells and was readily corrected by subtracting the original signal.

Images were captured on a Zeiss Examiner LSM880 confocal using a 20x/NA1.0 Plan Apochromat dipping objective. Embryos were typically imaged with X/Y pixel sizes of 0.59 µm and Z-step of 1.0 µm (speed = 8, bidirectional imaging, 1024 x 1024 pixels). Images were processed with Zen2.3 software and visualised as maximum projections (to show intensity) or 3D reconstructions (to show structure) in Fiji.

Myosin and tubulin imaging was performed on a Zeiss Examiner LSM880 confocal using a 20x/NA1.0 Plan Apochromat dipping objective with AiryScan Fast using FS (low zoom) or SR (high zoom) in-built settings.

In order to selectively visualise the apical surface (~3 µm deep into the tissue), our previously-described Surface Subtraction macro was used<sup>13,79</sup>. Images which have undergone this processing are described as being “surface-subtracted”.

### *Morphometric analyses*

PNP length, neural fold elevation and neuroepithelial cross-section analyses were performed in phalloidin wholemount or reflection-imaged PNPs as previously described<sup>13,21</sup>. To measure neuroepithelial thickness, transverse signal was enhanced post acquisition using sequential local contrast enhancement (CLAHE) in Fiji (block size 50, histogram bins 150, maximum slope 3 then repeated with block size 30, histogram bins 100, maximum slope 3) with 30 pixel rolling ball radius background subtraction before each CLAHE iteration.

## *Laser ablation and live embryo imaging*

Annular laser ablations were performed as previously reported<sup>21</sup> using a MaiTai laser (SpectraPhysics Mai Tai eHP DeepSee multiphoton laser, 30  $\mu\text{m}$  diameter ring at 710 nm wavelength, 80% laser power, 0.34  $\mu\text{s}$  pixel dwell time, 10 iterations). Embryos were dissected from the amnion, positioned in wells cut out of 4% agarose gel in DMEM, submerged in dissection medium and maintained at 37°C throughout imaging. Microsurgical needles from 11-0 Mersilene (TG140-6, Ethicon) and 10-0 Prolene (BV75-3, Ethicon) were used to hold the PNP pointing upwards. Cluster retraction was analysed by measuring the change in cluster area before and immediately after ablation using peripheral landmarks such as cell junctions to define cluster boundaries. Cell retraction was analysed by drawing around each cell before and immediately after ablation, then averaging the results for cells of the same type such that the embryo was used as the unit of measure. Illustrative particle image velocimetry (PIV) was performed in Fiji.

Live imaging was carried out using previously-described culture and imaging conditions<sup>12,44</sup>. Each embryo was positioned by making a small hole through the amnion and yolk sac and exteriorising the PNP to allow visualisation. A 10-0 Prolene microsurgical needle was curved through the allantois into agarose to keep the PNP pointing upwards and other needles were used to stop the yolk sac drifting onto it. The heart beat continued throughout imaging and the PNP commonly drifted as the embryo grew/deformed. Z-stacks of the neuroepithelium were captured once per minute and the field of view was re-centered after every two or three stacks. The resulting stacks were concatenated, processed with 5 iterations of Richardson-Lucy deconvolution using DeconvolutionLab, and 3D-registered in Fiji. Only cells which were present in all imaged time points were analyzed, in each case by manually identifying the last Z-slice in which the cell's apical surface was visible and drawing around it sequentially at every time point. While this is far more laborious than the commonly-used approach of selecting an optical cross-section for analysis, it is essential because the tissue curves during progression of closure. When analyzing PNPs with recombined cells, for each EGFP+ cells a "neighbor" and "distant" cell with similar initial morphology were selected for annotation. Cells which divided during imaging were not analyzed.

## *Statistical analysis*

Comparisons between two groups were by Student's t-test accounting for homogeneity of variance in Excel or in SPSS (IBM Statistics 22). Comparison of multiple groups was by one-way ANOVA with post-hoc Bonferroni in OriginPro 2017 (Origin Labs) which also tests normality and homogeneity of variance. Multivariate analysis was by linear mixed models in SPSS accounting for repeated measured from individual cells and embryos, and for multiple testing with a post-hoc Bonferroni. Graphs were made in OriginPro 2016 (Origin Labs) and are represented as box plots or as the mean  $\pm$  SEM when several groups are shown per measurement level.

Sample sizes for morphometric and laser ablation experiments were based on previous studies. A pilot study of quantifying apical constriction is described in the results. Blinding to CreERT2 positivity was generally not possible, but analyses were carried out without knowing whether embryos were Cre;Fl/Fl (no

phenotype) or Cre;Fl<sup>-</sup>. Thus, analyses were generally blinded to Vangl2 deletion status and no embryos were excluded after analysis. There were three exceptions to this blinding. The first exception is when Vangl2 itself was visualized given loss of Vangl2 signal was obvious in Cre;Fl<sup>-</sup> embryos only; these data are analyzed quantitatively. The second exception was when selecting embryos for live imaging. In order to ensure that control and experimental embryos were imaged, GLG inspected neural fold eversion, which by then was a recognized feature of Cre;Fl<sup>-</sup> embryos (note that this is only possible when the whole PNP can be seen, not when processing zoomed images of the apical neuroepithelium). This was only misjudged in one embryo. The third exception was AiryScan imaging of myosin and tubulin, for which only experimental embryos could be imaged due to processing limitations. To circumvent this, when quantifying tubulin tail length each tail was saved as a separate image with a blinded key indicating whether it was EGFP<sup>+</sup> or not.

$P < 0.05$  was considered statistically significant and all tests were two-tailed.

## Data availability

Values used to generate each graph are provided in the extended data. Unmerged or unprocessed images are provided in the extended data. All reagents are commercially available. In-house Fiji processing tools and related resources are available from the corresponding author on reasonable request.

## Declarations

## Acknowledgements

This study was funded partly by a Wellcome Trust Postdoctoral Clinical Research Training Fellowship (107474/Z/15/Z) and partly by a Wellcome Clinical Research Career Development Fellowship (211112/Z/18/Z), both to GLG. ARM was supported by a Child Health Research CIO award (to NDEG). AJC and NDEG are supported by Great Ormond Street Hospital Children's Charity. Research infrastructure within the institute is supported by the NIHR Great Ormond Street Hospital Biomedical Research Centre. The views expressed are those of the authors and not necessarily those of the NHS, the NIHR or the Department of Health. We thank Dr Dale Moulding for his help with image processing, as well as Dawn Savery and the biological services staff for help with transgenic colonies.

## Conflicts of interest

A.J.C. acts as paid consultant for ViiV Healthcare Limited, with fees going to support his research programme. The other authors declare no conflicts of interest.

## Author contributions

Conceptualization: GLG; Methodology: GLG, EM, ARM; Formal analysis: GLG, EM; Investigation: GLG, EM, ARM; Resources: GLG, NDEG, AJC; Data curation: GLG; Writing - original draft: GLG; Writing - review & editing: all authors; Visualization: G.L.G.; Supervision: GLG, NDEG, AJC; Project administration: GLG; Funding acquisition: GLG, NDEG, AJC.

## References

1. Zaganjor, I. *et al.* Describing the Prevalence of Neural Tube Defects Worldwide: A Systematic Literature Review. *PLoS One* **11**, e0151586, doi:10.1371/journal.pone.0151586 (2016).
2. Nikolopoulou, E., Galea, G. L., Rolo, A., Greene, N. D. & Copp, A. J. Neural tube closure: cellular, molecular and biomechanical mechanisms. *Development* **144**, 552-566, doi:10.1242/dev.145904 (2017).
3. van Straaten, H. W. & Copp, A. J. Curly tail: a 50-year history of the mouse spina bifida *Anat Embryol (Berl)* **203**, 225-237, doi:10.1007/s004290100169 (2001).
4. Greene, N. D., Leung, K. Y. & Copp, A. J. Inositol, neural tube closure and the prevention of neural tube defects. *Birth Defects Res* **109**, 68-80, doi:10.1002/bdra.23533 (2017).
5. Harris, M. J. & Juriloff, D. M. Mouse mutants with neural tube closure defects and their role in understanding human neural tube defects. *Birth Defects Res A Clin Mol Teratol* **79**, 187-210, doi:10.1002/bdra.20333 (2007).
6. Copp, A. J., Stanier, P. & Greene, N. D. Neural tube defects: recent advances, unsolved questions, and controversies. *Lancet Neurol* **12**, 799-810, doi:10.1016/S1474-4422(13)70110-8 (2013).
7. Robinson, A. *et al.* Mutations in the planar cell polarity genes CELSR1 and SCRIB are associated with the severe neural tube defect craniorachischisis. *Hum Mutat* **33**, 440-447, doi:10.1002/humu.21662 (2012).
8. Juriloff, D. M. & Harris, M. J. A consideration of the evidence that genetic defects in planar cell polarity contribute to the etiology of human neural tube defects. *Birth Defects Res A Clin Mol Teratol* **94**, 824-840, doi:10.1002/bdra.23079 (2012).
9. Kibar, Z. *et al.* Contribution of VANGL2 mutations to isolated neural tube defects. *Clin Genet* **80**, 76-82, doi:10.1111/j.1399-0004.2010.01515.x (2011).
10. Tian, T. *et al.* Somatic mutations in planar cell polarity genes in neural tissue from human fetuses with neural tube defects. *Hum Genet*, doi:10.1007/s00439-020-02172-0 (2020).
11. Erickson, R. P. Somatic gene mutation and human disease other than cancer: an update. *Mutat Res* **705**, 96-106, doi:10.1016/j.mrrev.2010.04.002 (2010).
12. Galea, G. L. *et al.* Biomechanical coupling facilitates spinal neural tube closure in mouse embryos. *Proc Natl Acad Sci U S A* **114**, E5177-E5186, doi:10.1073/pnas.1700934114 (2017).
13. Galea, G. L. *et al.* Vangl2 disruption alters the biomechanics of late spinal neurulation leading to spina bifida in mouse embryos. *Dis Model Mech* **11**, doi:10.1242/dmm.032219 (2018).

14. Ybot-Gonzalez, P. *et al.* Convergent extension, planar-cell-polarity signalling and initiation of mouse neural tube closure. *Development* **134**, 789-799, doi:10.1242/dev.000380 (2007).
15. Torban, E., Wang, H. J., Groulx, N. & Gros, P. Independent mutations in mouse Vangl2 that cause neural tube defects in looptail mice impair interaction with members of the Dishevelled family. *J Biol Chem* **279**, 52703-52713, doi:10.1074/jbc.M408675200 (2004).
16. Wang, L. *et al.* Digenic variants of planar cell polarity genes in human neural tube defect patients. *Mol Genet Metab* **124**, 94-100, doi:10.1016/j.ymgme.2018.03.005 (2018).
17. Aw, W. Y. & Devenport, D. Planar cell polarity: global inputs establishing cellular *Curr Opin Cell Biol* **44**, 110-116, doi:10.1016/j.ceb.2016.08.002 (2017).
18. Ezan, J. & Montcouquiol, M. Revisiting planar cell polarity in the inner ear. *Semin Cell Dev Biol* **24**, 499-506, doi:10.1016/j.semcdb.2013.03.012 (2013).
19. Phillips, H. M. *et al.* Non-cell-autonomous roles for the planar cell polarity gene Vangl2 in development of the coronary circulation. *Circ Res* **102**, 615-623, doi:10.1161/CIRCRESAHA.107.160861 (2008).
20. Strutt, H. & Strutt, D. Nonautonomous planar polarity patterning in Drosophila: dishevelled-independent functions of frizzled. *Dev Cell* **3**, 851-863, doi:10.1016/s1534-5807(02)00363-5 (2002).
21. Butler, M. B. *et al.* Rho kinase-dependent apical constriction counteracts M-phase apical expansion to enable mouse neural tube *J Cell Sci* **132**, doi:10.1242/jcs.230300 (2019).
22. McGreevy, E. M., Vijayraghavan, D., Davidson, L. A. & Hildebrand, J. D. Shroom3 functions downstream of planar cell polarity to regulate myosin II distribution and cellular organization during neural tube closure. *Biol Open* **4**, 186-196, doi:10.1242/bio.20149589 (2015).
23. Ossipova, O., Chuykin, I., Chu, C. W. & Sokol, S. Y. Vangl2 cooperates with Rab11 and Myosin V to regulate apical constriction during vertebrate gastrulation. *Development* **142**, 99-107, doi:10.1242/dev.111161 (2015).
24. Ossipova, O., Kim, K. & Sokol, S. Y. Planar polarization of Vangl2 in the vertebrate neural plate is controlled by Wnt and Myosin II signaling. *Biol Open* **4**, 722-730, doi:10.1242/bio.201511676 (2015).
25. Nishimura, T., Honda, H. & Takeichi, M. Planar cell polarity links axes of spatial dynamics in neural-tube closure. *Cell* **149**, 1084-1097, doi:10.1016/j.cell.2012.04.021 (2012).
26. An, Y. *et al.* Apical constriction is driven by a pulsatile apical myosin network in delaminating Drosophila neuroblasts. *Development* **144**, 2153-2164, doi:10.1242/dev.150763 (2017).
27. Vasquez, C. G., Tworoger, M. & Martin, A. C. Dynamic myosin phosphorylation regulates contractile pulses and tissue integrity during epithelial morphogenesis. *J Cell Biol* **206**, 435-450, doi:10.1083/jcb.201402004 (2014).
28. Martin, A. C. & Goldstein, B. Apical constriction: themes and variations on a cellular mechanism driving morphogenesis. *Development* **141**, 1987-1998, doi:10.1242/dev.102228 (2014).
29. Shindo, A., Inoue, Y., Kinoshita, M. & Wallingford, J. B. PCP-dependent transcellular regulation of actomyosin oscillation facilitates convergent extension of vertebrate tissue. *Dev Biol* **446**, 159-167,

- doi:10.1016/j.ydbio.2018.12.017 (2019).
30. Corrigall, D., Walther, R. F., Rodriguez, L., Fichelson, P. & Pichaud, F. Hedgehog signaling is a principal inducer of Myosin-II-driven cell ingression in *Drosophila* epithelia. *Dev Cell* **13**, 730-742, doi:10.1016/j.devcel.2007.09.015 (2007).
  31. Lee, C., Scherr, H. M. & Wallingford, J. B. Shroom family proteins regulate gamma-tubulin distribution and microtubule architecture during epithelial cell shape change. *Development* **134**, 1431-1441, doi:10.1242/dev.02828 (2007).
  32. Lee, J. Y. & Harland, R. M. Actomyosin contractility and microtubules drive apical constriction in *Xenopus* bottle cells. *Dev Biol* **311**, 40-52, doi:10.1016/j.ydbio.2007.08.010 (2007).
  33. Booth, A. J. R., Blanchard, G. B., Adams, R. J. & Roper, K. A dynamic microtubule cytoskeleton directs medial actomyosin function during tube formation. *Dev Cell* **29**, 562-576, doi:10.1016/j.devcel.2014.03.023 (2014).
  34. Fernandes, V. M., McCormack, K., Lewellyn, L. & Verheyen, E. M. Integrins regulate apical constriction via microtubule stabilization in the *Drosophila* eye disc epithelium. *Cell Rep* **9**, 2043-2055, doi:10.1016/j.celrep.2014.11.041 (2014).
  35. Singh, A. *et al.* Polarized microtubule dynamics directs cell mechanics and coordinates forces during epithelial morphogenesis. *Nat Cell Biol* **20**, 1126-1133, doi:10.1038/s41556-018-0193-1 (2018).
  36. Chen, H., Xiao, X., Lui, W. Y., Lee, W. M. & Cheng, C. Y. Vangl2 regulates spermatid planar cell polarity through microtubule (MT)-based cytoskeleton in the rat testis. *Cell Death Dis* **9**, 340, doi:10.1038/s41419-018-0339-x (2018).
  37. Jarjour, A. A. *et al.* The formation of paranodal spirals at the ends of CNS myelin sheaths requires the planar polarity protein Vangl2. *Glia*, doi:10.1002/glia.23809 (2020).
  38. Brown, J. M. & Garcia-Garcia, M. J. Secretory pathway calcium ATPase 1 (SPCA1) controls mouse neural tube closure by regulating cytoskeletal dynamics. *Development* **145**, doi:10.1242/dev.170019 (2018).
  39. Sulistomo, H. W., Nemoto, T., Yanagita, T. & Takeya, R. Formin homology 2 domain-containing 3 (Fhod3) controls neural plate morphogenesis in mouse cranial neurulation by regulating multidirectional apical constriction. *J Biol Chem* **294**, 2924-2934, doi:10.1074/jbc.RA118.005471 (2019).
  40. Escuin, S. *et al.* Rho-kinase-dependent actin turnover and actomyosin disassembly are necessary for mouse spinal neural tube. *J Cell Sci* **128**, 2468-2481, doi:10.1242/jcs.164574 (2015).
  41. Grego-Bessa, J., Hildebrand, J. & Anderson, K. V. Morphogenesis of the mouse neural plate depends on distinct roles of cofilin 1 in apical and basal epithelial domains. *Development* **142**, 1305-1314, doi:10.1242/dev.115493 (2015).
  42. Christodoulou, N. & Skourides, P. A. Cell-Autonomous Ca(2+) Flashes Elicit Pulsed Contractions of an Apical Actin Network to Drive Apical Constriction during Neural Tube Closure. *Cell Rep* **13**, 2189-2202, doi:10.1016/j.celrep.2015.11.017 (2015).

43. Williams, M., Yen, W., Lu, X. & Sutherland, A. Distinct apical and basolateral mechanisms drive planar cell polarity-dependent convergent extension of the mouse neural plate. *Dev Cell* **29**, 34- 46, doi:10.1016/j.devcel.2014.02.007 (2014).
44. Mole, M. A. *et al.* Integrin-Mediated Focal Anchorage Drives Epithelial Zippering during Mouse Neural Tube Closure. *Dev Cell* **52**, 321-334 e326, doi:10.1016/j.devcel.2020.01.012 (2020).
45. Ved, N., Curran, A., Ashcroft, F. M. & Sparrow, D. B. Tamoxifen administration in pregnant mice can be deleterious to both mother and embryo. *Lab Anim* **53**, 630-633, doi:10.1177/0023677219856918 (2019).
46. Savery, D. *et al.* Refinement of inducible gene deletion in embryos of pregnant mice. *Birth Defects Res* **112**, 196-204, doi:10.1002/bdr2.1628 (2020).
47. Mugele, D. *et al.* Genetic approaches in mice demonstrate that neuro-mesodermal progenitors express *T/Brachyury* but not *Sox2*. *bioRxiv*, 503854, doi:10.1101/503854 (2018).
48. Rodrigo Albors, A., Halley, P. A. & Storey, K. G. Lineage tracing of axial progenitors using *Nkx1-2CreER(T2)* mice defines their trunk and tail contributions. *Development* **145**, doi:10.1242/dev.164319 (2018).
49. Dos-Santos Carvalho, S. *et al.* *Vangl2* acts at the interface between actin and N-cadherin to modulate mammalian neuronal outgrowth. *Elife* **9**, doi:10.7554/eLife.51822 (2020).
50. Mathewson, A. W., Berman, D. G. & Moens, C. B. Microtubules are required for the maintenance of planar cell polarity in monociliated floorplate cells. *Dev Biol* **452**, 21-33, doi:10.1016/j.ydbio.2019.04.007 (2019).
51. Ito, S. *et al.* Induced cortical tension restores functional junctions in adhesion-defective carcinoma cells. *Nat Commun* **8**, 1834, doi:10.1038/s41467-017-01945-y (2017).
52. Ko, C. S., Tserunyan, V. & Martin, A. C. Microtubules promote intercellular contractile force transmission during tissue folding. *J Cell Biol* **218**, 2726-2742, doi:10.1083/jcb.201902011 (2019).
53. Lewis, F. T. The effect of cell division on the shape and size of hexagonal cells. *Anat Rec* **33**, 331-355, doi:DOI 10.1002/ar.1090330502 (1926).
54. Kim, S., Cai, M. & Hilgenfeldt, S. Lewis' law revisited: the role of anisotropy in size-topology correlations. *New J Phys* **16**, doi:10.1088/1367-2630/16/1/015024 (2014).
55. De, S. Somatic mosaicism in healthy human tissues. *Trends Genet* **27**, 217-223, doi:10.1016/j.tig.2011.03.002 (2011).
56. Campbell, I. M., Shaw, C. A., Stankiewicz, P. & Lupski, J. R. Somatic mosaicism: implications for disease and transmission genetics. *Trends Genet* **31**, 382-392, doi:10.1016/j.tig.2015.03.013 (2015).
57. Bae, T. *et al.* Different mutational rates and mechanisms in human cells at pregastrulation and neurogenesis. *Science* **359**, 550-555, doi:10.1126/science.aan8690 (2018).
58. Lim, Y. H., Moscato, Z. & Choate, K. A. Mosaicism in Cutaneous Disorders. *Annu Rev Genet* **51**, 123-141, doi:10.1146/annurev-genet-121415-121955 (2017).

59. Asch, S. & Sugarman, J. L. Epidermal nevus syndromes. *Handb Clin Neurol* **132**, 291-316, doi:10.1016/B978-0-444-62702-5.00022-6 (2015).
60. Manheimer, K. B. *et al.* Robust identification of mosaic variants in congenital heart disease. *Hum Genet* **137**, 183-193, doi:10.1007/s00439-018-1871-6 (2018).
61. Wright, C. F. *et al.* Clinically-relevant postzygotic mosaicism in parents and children with developmental disorders in trio exome sequencing data. *Nat Commun* **10**, 2985, doi:10.1038/s41467-019-11059-2 (2019).
62. Tzouanacou, E., Wegener, A., Wymeersch, F. J., Wilson, V. & Nicolas, J. F. Redefining the progression of lineage segregations during mammalian embryogenesis by clonal analysis. *Dev Cell* **17**, 365-376, doi:10.1016/j.devcel.2009.08.002 (2009).
63. Henrique, D., Abranches, E., Verrier, L. & Storey, K. G. Neuromesodermal progenitors and the making of the spinal cord. *Development* **142**, 2864-2875, doi:10.1242/dev.119768 (2015).
64. Rolo, A. *et al.* Regulation of cell protrusions by small GTPases during fusion of the neural *Elife* **5**, e13273, doi:10.7554/eLife.13273 (2016).
65. Murdoch, J. N. *et al.* Genetic interactions between planar cell polarity genes cause diverse neural tube defects in mice. *Dis Model Mech* **7**, 1153-1163, doi:10.1242/dmm.016758 (2014).
66. Humphries, A. C., Narang, S. & Mlodzik, M. Mutations associated with human neural tube defects display disrupted planar cell polarity in *Drosophila*. *Elife* **9**, doi:10.7554/eLife.53532 (2020).
67. Fisher, K. H. & Strutt, D. A theoretical framework for planar polarity establishment through interpretation of graded cues by molecular bridges. *Development* **146**, doi:10.1242/dev.168955 (2019).
68. Strutt, H. & Strutt, D. Asymmetric localisation of planar polarity proteins: Mechanisms and consequences. *Semin Cell Dev Biol* **20**, 957-963, doi:10.1016/j.semcdb.2009.03.006 (2009).
69. Aw, W. Y., Heck, B. W., Joyce, B. & Devenport, D. Transient Tissue-Scale Deformation Coordinates Alignment of Planar Cell Polarity Junctions in the Mammalian Skin. *Curr Biol* **26**, 2090-2100, doi:10.1016/j.cub.2016.06.030 (2016).
70. Shi, D. *et al.* Dynamics of planar cell polarity protein Vangl2 in the mouse oviduct *Mech Dev* **141**, 78-89, doi:10.1016/j.mod.2016.05.002 (2016).
71. Belotti, E. *et al.* Molecular characterisation of endogenous Vangl2/Vangl1 heteromeric protein complexes. *PLoS One* **7**, e46213, doi:10.1371/journal.pone.0046213 (2012).
72. Pryor, S. E. *et al.* Vangl-dependent planar cell polarity signalling is not required for neural crest migration in mammals. *Development* **141**, 3153-3158, doi:10.1242/dev.111427 (2014).
73. McShane, S. G. *et al.* Cellular basis of neuroepithelial bending during mouse spinal neural tube closure. *Dev Biol* **404**, 113-124, doi:10.1016/j.ydbio.2015.06.003 (2015).
74. Seo, H. S., Habas, R., Chang, C. & Wang, J. Bimodal regulation of Dishevelled function by Vangl2 during morphogenesis. *Hum Mol Genet* **26**, 2053-2061, doi:10.1093/hmg/ddx095 (2017).

75. Lopez-Escobar, B. *et al.* The non-canonical Wnt-PCP pathway shapes the mouse caudal neural plate. *Development* **145**, doi:10.1242/dev.157487 (2018).
76. Sai, X., Yonemura, S. & Ladher, R. K. Junctionally restricted RhoA activity is necessary for apical constriction during phase 2 inner ear placode invagination. *Dev Biol* **394**, 206-216, doi:10.1016/j.ydbio.2014.08.022 (2014).
77. Dady, A., Blavet, C. & Duband, J. L. Timing and kinetics of E- to N-cadherin switch during neurulation in the avian embryo. *Dev Dyn* **241**, 1333-1349, doi:10.1002/dvdy.23813 (2012).
78. Panorchan, P. *et al.* Single-molecule analysis of cadherin-mediated cell-cell adhesion. *J Cell Sci* **119**, 66-74, doi:10.1242/jcs.02719 (2006).
79. Nikolopoulou, E. *et al.* Spinal neural tube closure depends on regulation of surface ectoderm identity and biomechanics by Grhl2. *Nat Commun* **10**, 2487, doi:10.1038/s41467-019-10164-6 (2019).
80. Chuykin, I., Ossipova, O. & Sokol, S. Y. Par3 interacts with Prickle3 to generate apical PCP complexes in the vertebrate neural plate. *Elife* **7**, doi:10.7554/eLife.37881 (2018).
81. Butler, M. T. & Wallingford, J. B. Spatial and temporal analysis of PCP protein dynamics during neural tube closure. *Elife* **7**, doi:10.7554/eLife.36456 (2018).
82. Ossipova, O. *et al.* Role of Rab11 in planar cell polarity and apical constriction during vertebrate neural tube closure. *Nat Commun* **5**, 3734, doi:10.1038/ncomms4734 (2014).
83. Laevsky, G. & Knecht, D. A. Cross-linking of actin filaments by myosin II is a major contributor to cortical integrity and cell motility in restrictive environments. *J Cell Sci* **116**, 3761-3770, doi:10.1242/jcs.00684 (2003).
84. Xu, X. S. *et al.* During multicellular migration, myosin ii serves a structural role independent of its motor function. *Dev Biol* **232**, 255-264, doi:10.1006/dbio.2000.0132 (2001).
85. Yvon, A. M., Gross, D. J. & Wadsworth, P. Antagonistic forces generated by myosin II and cytoplasmic dynein regulate microtubule turnover, movement, and organization in interphase cells. *Proc Natl Acad Sci U S A* **98**, 8656-8661, doi:10.1073/pnas.141224198 (2001).
86. Cao, T. T., Chang, W., Masters, S. E. & Mooseker, M. S. Myosin-Va binds to and mechanochemically couples microtubules to actin filaments. *Mol Biol Cell* **15**, 151-161, doi:10.1091/mbc.e03-07-0504 (2004).
87. Karfunkel, P. The role of microtubules and microfilaments in neurulation in *Xenopus*. *Dev Biol* **25**, 30-56, doi:10.1016/0012-1606(71)90018-2 (1971).
88. Suzuki, M., Hara, Y., Takagi, C., Yamamoto, T. S. & Ueno, N. MID1 and MID2 are required for *Xenopus* neural tube closure through the regulation of microtubule organization. *Development* **137**, 2329-2339, doi:10.1242/dev.048769 (2010).
89. Inoue, Y. *et al.* Mechanical roles of apical constriction, cell elongation, and cell migration during neural tube formation in *Xenopus*. *Biomech Model Mechanobiol* **15**, 1733-1746, doi:10.1007/s10237-016-0794-1 (2016).

90. Suzuki, M., Morita, H. & Ueno, N. Molecular mechanisms of cell shape changes that contribute to vertebrate neural tube closure. *Dev Growth Differ* **54**, 266-276, doi:10.1111/j.1440-169X.2012.01346.x (2012).
91. Matis, M., Russler-Germain, D. A., Hu, Q., Tomlin, C. J. & Axelrod, J. D. Microtubules provide directional information for core PCP function. *Elife* **3**, e02893, doi:10.7554/eLife.02893 (2014).
92. Balashova, O. A., Visina, O. & Borodinsky, L. N. Folate receptor 1 is necessary for neural plate cell apical constriction during *Xenopus* neural tube formation. *Development* **144**, 1518-1530, doi:10.1242/dev.137315 (2017).
93. Martin, J. B., Muccioli, M., Herman, K., Finnell, R. H. & Plageman, T. F., Jr. Folic acid modifies the shape of epithelial cells during morphogenesis via a Folr1 and MLCK dependent mechanism. *Biol Open* **8**, doi:10.1242/bio.041160 (2019).
94. Wang, B. *et al.* Levels of polycyclic aromatic hydrocarbons in maternal serum and risk of neural tube defects in offspring. *Environ Sci Technol* **49**, 588-596, doi:10.1021/es503990v (2015).
95. Wang, L. *et al.* Indoor air pollution and neural tube defects: effect modification by maternal genes. *Epidemiology* **25**, 658-665, doi:10.1097/EDE.000000000000129 (2014).
96. Bai, H., Wu, M., Zhang, H. & Tang, G. Chronic polycyclic aromatic hydrocarbon exposure causes DNA damage and genomic instability in lung epithelial cells. *Oncotarget* **8**, 79034-79045, doi:10.18632/oncotarget.20891 (2017).
97. Swayne, B. G. *et al.* Investigating the effects of dietary folic acid on sperm count, DNA damage and mutation in Balb/c *Mutat Res* **737**, 1-7, doi:10.1016/j.mrfmmm.2012.07.002 (2012).
98. Beetstra, S., Thomas, P., Salisbury, C., Turner, J. & Fenech, M. Folic acid deficiency increases chromosomal instability, chromosome 21 aneuploidy and sensitivity to radiation-induced micronuclei. *Mutat Res* **578**, 317-326, doi:10.1016/j.mrfmmm.2005.05.012 (2005).
99. Binici, D. N., Karaman, A., Coskun, M., Oglu, A. U. & Ucar, F. Genomic damage in patients with type-2 diabetes mellitus. *Genet Couns* **24**, 149-156 (2013).
100. Attia, S. M., Helal, G. K. & Alhaider, A. A. Assessment of genomic instability in normal and diabetic rats treated with metformin. *Chem Biol Interact* **180**, 296-304, doi:10.1016/j.cbi.2009.03.001 (2009).
101. Mowla, S., Gissler, M., Raisanen, S. & Kancherla, V. Association between maternal pregestational diabetes mellitus and spina bifida: A population-based case-control study, Finland, 2000-2014. *Birth Defects Res* **112**, 186-195, doi:10.1002/bdr2.1624 (2020).
102. Anderson, J. L. *et al.* Maternal obesity, gestational diabetes, and central nervous system birth defects. *Epidemiology* **16**, 87-92, doi:10.1097/01.ede.0000147122.97061.bb (2005).
103. Camerer, E. *et al.* Local protease signaling contributes to neural tube closure in the mouse embryo. *Developmental cell* **18**, 25-38, doi:10.1016/j.devcel.2009.11.014 (2010).
104. Ramsbottom, S. A. *et al.* Vangl2-regulated polarisation of second heart field-derived cells is required for outflow tract lengthening during cardiac development. *PLoS genetics* **10**, e1004871, doi:10.1371/journal.pgen.1004871 (2014).

105. Pryor, S. E., Massa, V., Savery, D., Greene, N. D. & Copp, A. J. Convergent extension analysis in mouse whole embryo culture. *Methods in molecular biology* **839**, 133-146, doi:10.1007/978-1-61779-510-7\_11 (2012).

## Figures

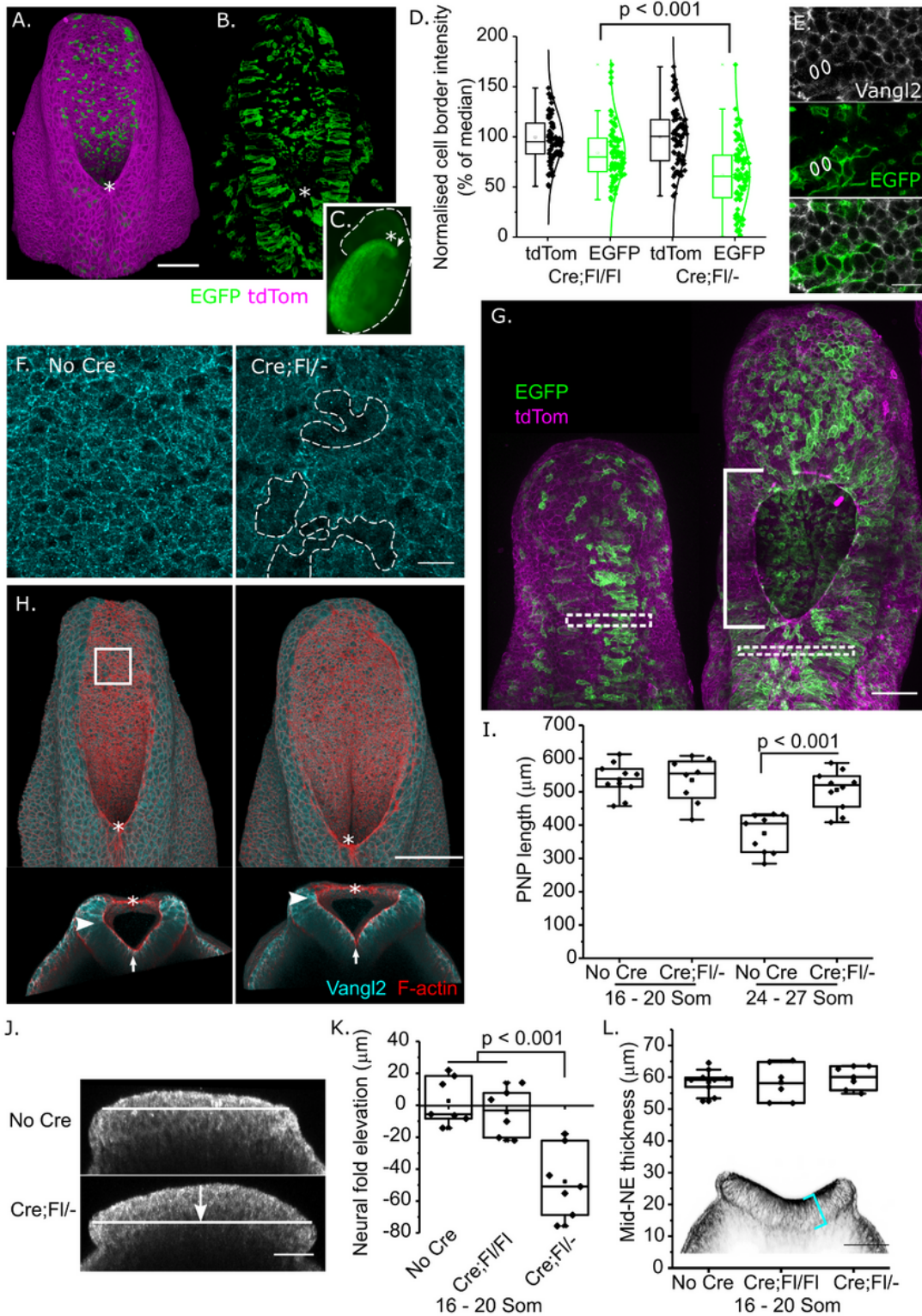
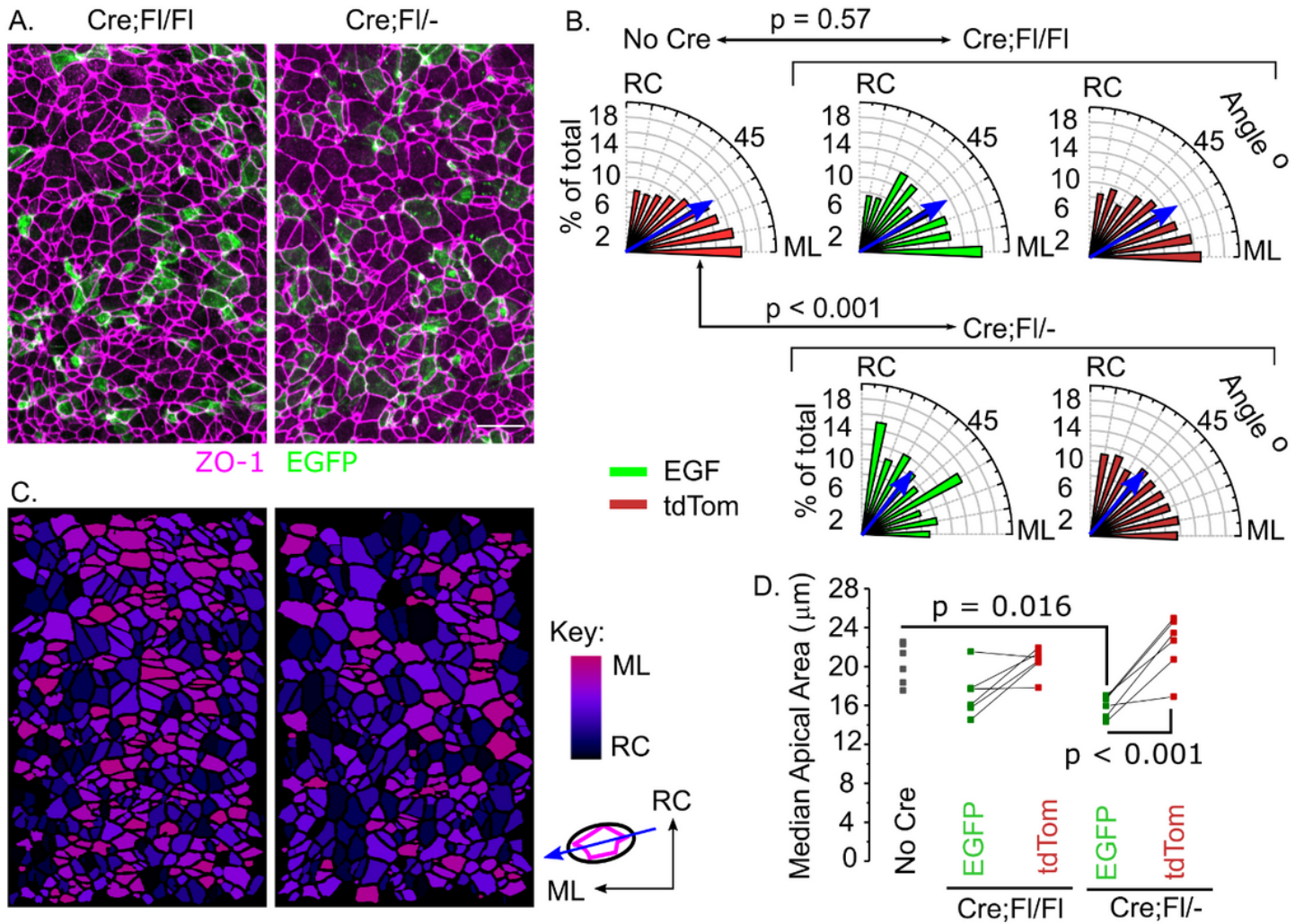


Figure 1

Mosaic Vangl2 deletion prevents neural fold elevation, leading to diminished PNP shortening and ultimately failure of closure. A,B. Representative PNP 3D reconstructions illustrating Nkx1.2CreERT2 lineage tracing using the mTmG reporter. In B, non-recombined cells which continue to express tdTom are not shown. Scale = 100  $\mu$ m. C. Fluorescence image of an E9.5 Nkx1.2CreERT2 lineage traced embryo showing persistent EGFP expression in the PNP (arrow) as well as in the closed neural tube to upper spinal level. \* denotes zippering point, dashed line indicates the embryo outline. D. Quantification of Vangl2 immunolocalisation on cell borders lineage traced with EGFP or tdTom (not recombined) in Cre;Fl/Fl and Cre;Fl/- embryos. The average Vangl2 intensity in non-recombined (tdTom) cells was set at 100% in each embryo (4 embryos from independent litters per genotype). E. Optical cross-section through the neuroepithelium of a Cre;Fl/- embryo showing endogenous EGFP and immunofluorescently-detected Vangl2. White circles indicate borders between two EGFP+ cells, which are devoid of Vangl2 signal. Scale = 20  $\mu$ m. F. Surface-subtracted wholemount immunolocalisation of Vangl2 in the apical neuroepithelium of control (henceforth labelled "No Cre") and Cre;Fl/- embryo, showing mosaic deletion (example regions demarcated by white dotted lines) in the latter. Scale = 20  $\mu$ m. G. Representative images of two E10.5 Cre;Fl/- embryos with low (left) and high (right) recombination assessed from EGFP expression. Left: 37 somites, successful PNP closure has occurred. Right: 39 somites, tile-scanned image of failed PNP closure producing a pre-spina bifida lesion (white bracket). Dashed white boxes denote comparable regions of closed neural tube where recombination was quantified in optical cross-sections in Supplementary Figure 2C. H. 3D reconstructions of a No Cre (left) and Cre;Fl/- (right) PNP from embryos collected at E9.5 showing the dorsolateral hinge points (arrowhead) and medial hinge point (arrow). White box indicates the region of flat neural plate shown in F. \* denotes zippering point. I. Quantification of PNP length in control and Cre;Fl/- embryos at the indicated somite stages (E9-E9.5). J. Optical cross-sections through the caudal PNP (at 75% of rostrocaudal PNP length) of No Cre and Cre;Fl/- embryos at E9.5, visualised using reflection imaging. The white arrow indicates the quantified eversion of the apical neuroepithelium, which should elevate its lateral margins to form neural folds. K,L. Quantification of neural fold elevation (K; positive values) or eversion (K; negative values) and mid-PNP neuroepithelial thickness (L) in control, Cre;Fl/Fl and Cre;Fl/- embryos at 16-20 somite stages, before the PNP is significantly longer in Cre;Fl/- embryos. The inset shows an optical cross-section through a phalloidin-stained PNP indicating the thickness of the neuroepithelium (cyan bracket) In each case tamoxifen was administered 24-30 hrs prior to collection. P values from ANOVA with post-hoc Bonferroni.



**Figure 2**

Mosaic Vangl2 deletion disrupts planar polarised neuroepithelial apical orientation. A. Representative surface-subtracted images of the apical neuroepithelium in a Cre;Fl/Fl embryo and Cre;Fl/- littermate showing the apical marker Zo-1 and recombined cells lineage traced with EGFP. B. Quantification of the orientation of the apical long axis of neuroepithelial cells in No Cre, Cre;Fl/Fl and Cre;Fl/- embryos. Blue arrows indicate the median orientation; p values from Chi2 with Yates continuity correction; EGFP and tdTom not significantly different within genotypes. No Cre 5,592 cells from 6 embryos; Cre;Fl/Fl EGFP/tdTom 318/2373 cells from 5 embryos; Cre;Fl/- EGFP/tdTom 267/3799 cells from 6 embryos. RC = rostrocaudal, ML = mediolateral. C. Apical surfaces from A colour coded to illustrate orientation. D. Quantification of neuroepithelial apical area. Each point represents the median value for an embryo and lines link points from the same embryo. P values from ANOVA with post-hoc Bonferroni. Embryos compared had 15-20 somites and had been administered tamoxifen 24-28 h prior to analysis.

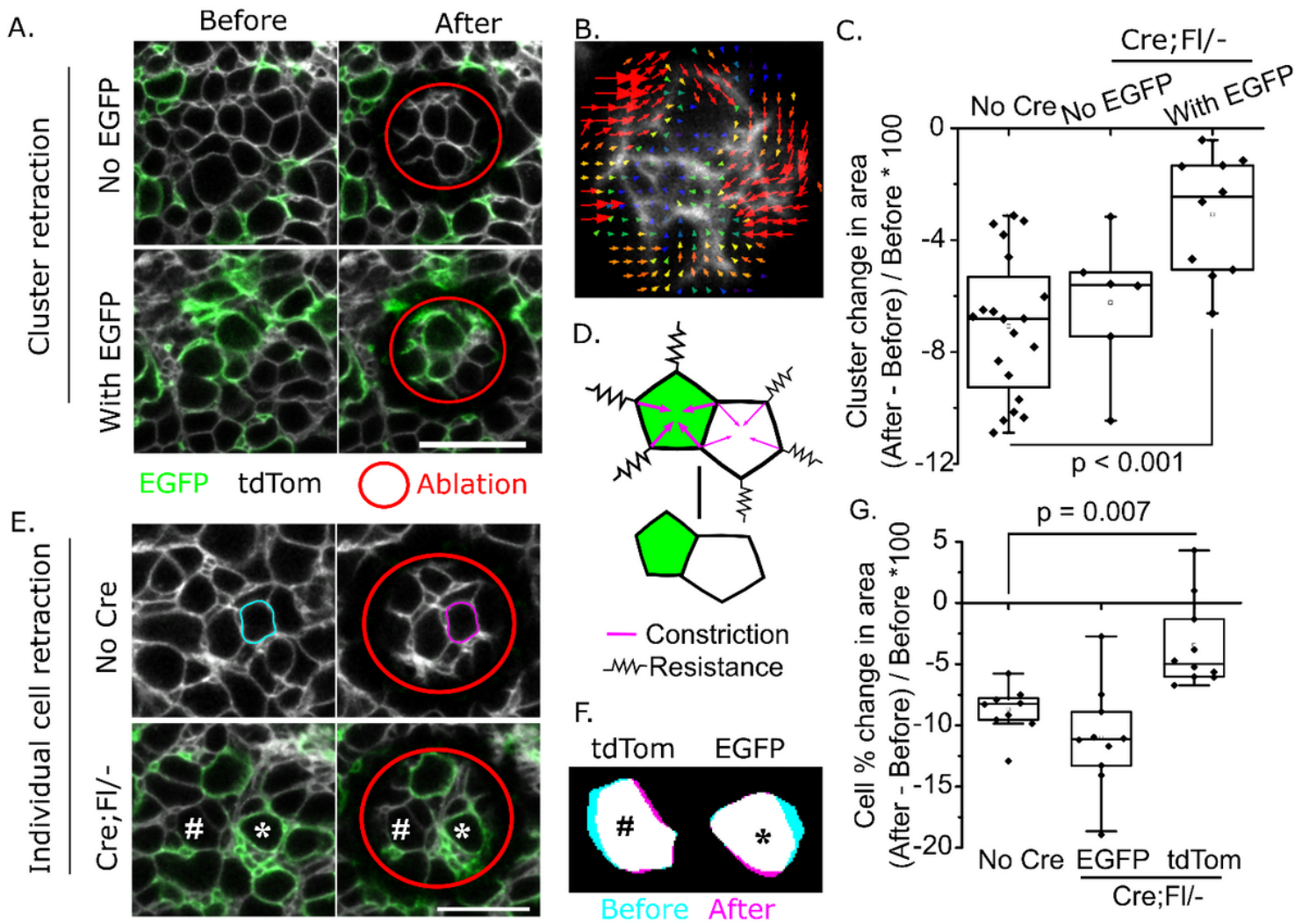


**Figure 3**

Mosaic Vangl2 deletion non-autonomously diminishes neuroepithelial apical retraction. A. Representative live-imaged neuroepithelium before and after annular laser ablation. Ablations were made in regions including (with EGFP) or excluding (no EGFP) Vangl2-deleted cells. B. Particle image velocimetry (arrows superimposed on grey cell borders) illustrating apical retraction of a cluster of cells within the ablated annulus. C. Quantification of the retraction (% change in area) of cell clusters within the ablated annulus. Dots represent a cluster in an individual embryo; each embryo was only ablated once. D. Schematic illustration of cell retraction due to immediate constriction when released from connections to surrounding cells. E, F. Representative live-imaged neuroepithelium from a control (No Cre) and Cre;Fl/- embryo. A cell is traced before and after ablation in the No Cre control. The # and \* correspond to the cells shown in F, illustrating retraction. G. Quantification of the retraction (% change in area) of individual cells within the ablated annulus. Ablations included 2-3 Vangl2-deleted (EGFP) and Vangl2-replete (tdTom) neighbours of the deleted cells. Retractions of cells of the same type were averaged in each cluster so embryos are the unit of measure rather than cells. Scale bars = 20  $\mu\text{m}$ . P values from ANOVA with post-hoc Bonferroni.

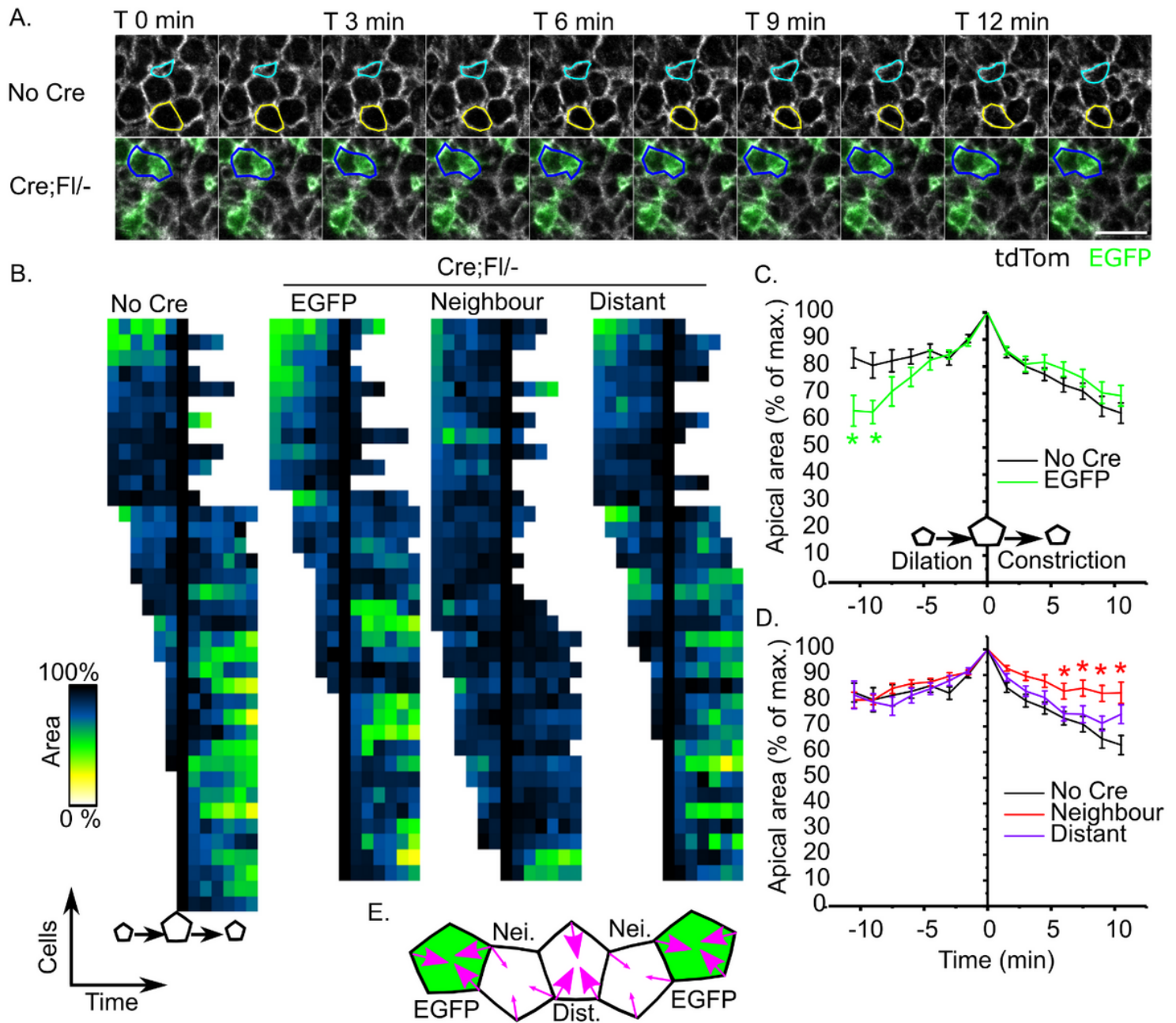


**Figure 4**

Vangl2-replete neighbours of Vangl2-deleted cells fail to apically constrict. **A.** Representative live-imaged sequences of No Cre and Cre;Fl/- embryos. Cyan: Apically-expanding cell. Yellow: Apically constricting cell. Blue: Constricting then partly dilating Vangl2-deleted (EGFP+) cell. Scale bar = 20  $\mu$ m. **B.** Heat maps illustrating the change in apical areas of each analysed cell in No Cre and Cre;Fl/- embryos. Dark colours indicate large apical areas (up to 100% of observed sizes). **C,D.** Quantification of changes in cells' apical areas during live imaging. **C:** No Cre compared with EGFP recombined cells. **D:** No Cre compared with cells neighbouring EGFP recombined cells, and more distant cells that do not contact EGFP recombined cells. Each cell is aligned at T = 0 when it reaches the biggest observed apical area. Negative time points represent increasing apical areas (dilation), positive time points represent constriction. \* indicate p < 0.05

at each indicated time point by mixed model analysis with Bonferroni post-hoc. No Cre: 38 cells from 5 embryos, Cre;Fl/- 36 cells of each type from 5 embryos. E. Schematic illustration of the live imaging and laser ablation results. EGFP+Vangl2- cells constrict/retract similarly to cells in control embryos. EGFP-Vangl2+ neighbours (Nei.) of Vangl2-deleted cells do not constrict/retract. EGFP-Vangl2+ distant (Dist.) cells which do not contact Vangl2-deleted cells constrict/retract normally. Magenta arrow thickness indicates constriction magnitude.

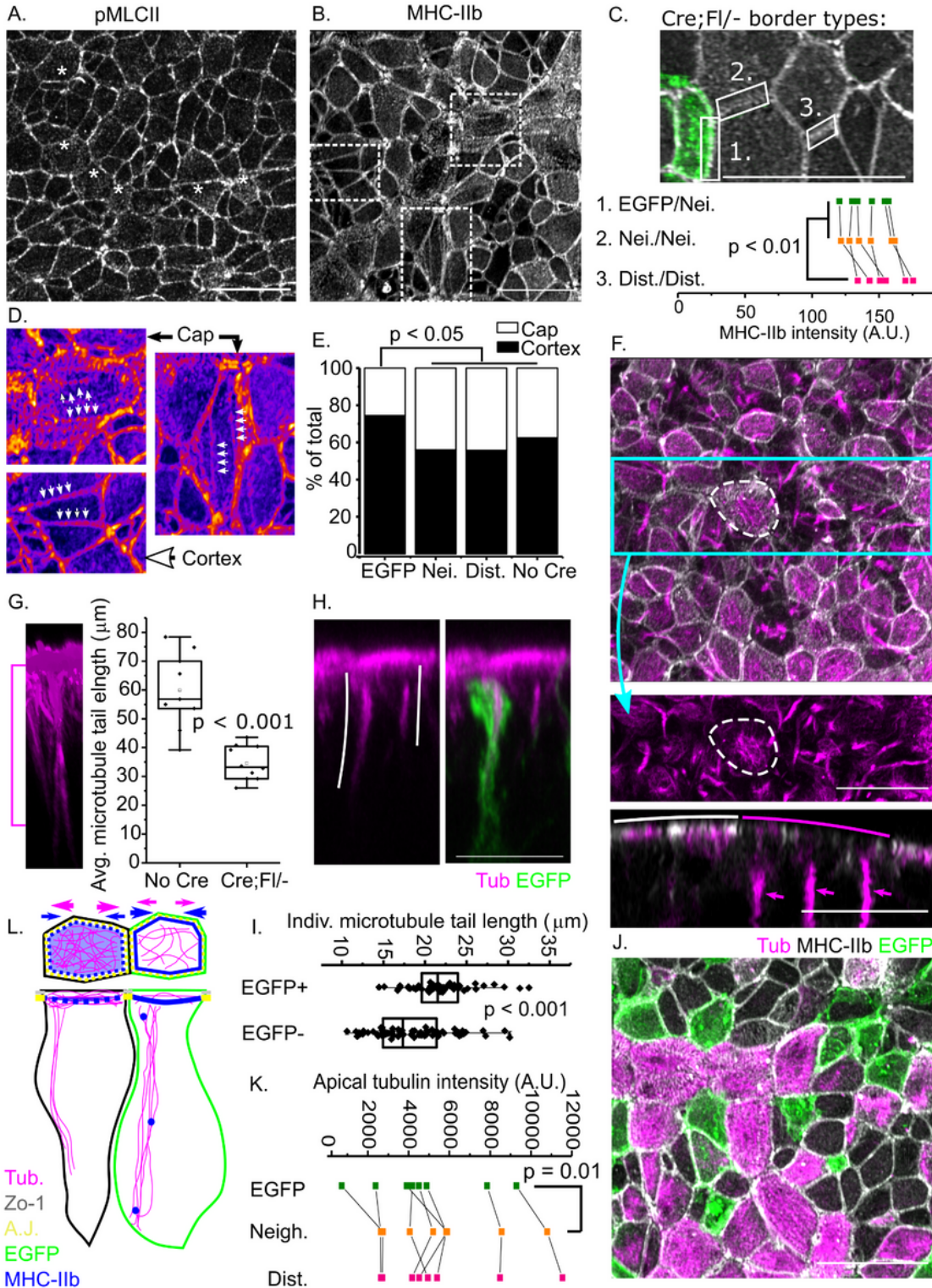
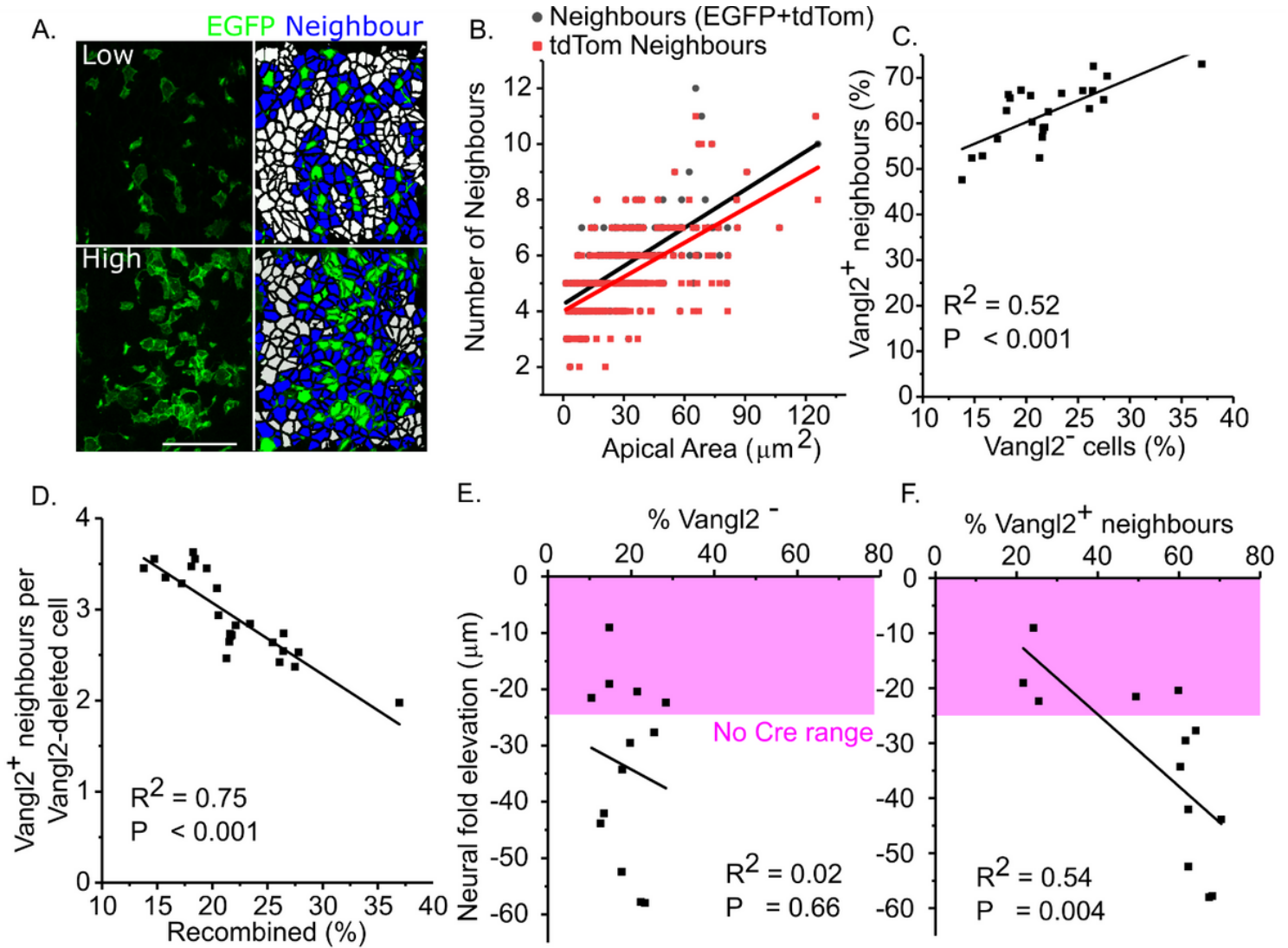


Figure 5

Autonomous and non-autonomous cytoskeletal changes may underlie diminished apical constriction. A,B. Surface-subtracted wholemount images showing pMLCII (A) and total MHC-IIb (B) on the apical neuroepithelium of control embryos. \*: apical staining. Dashed boxes indicate the cells shown in D. C. Quantification of MHC-IIb intensity along three types of cell-cell borders indicated by the white boxes. 1: EGFP-Neighbour, 2: Neighbour-Neighbour, 3: Distant-Distant. Lines indicate average intensity values from the same embryo, compared by repeated measures ANOVA. D. Representative cells showing apical cap stress-fibre or sarcomere-like arrangements (Cap) or primarily cortical (Cortex) MHC-IIb staining. Fire LUT used to emphasize low and high staining intensities. Arrows indicate the two types of MHC-IIb staining. E. Quantification of the proportion of cells with primarily cortical or primarily apical cap MHC-IIb. P values by X2. Cre;Fl/- EGFP = 98 cells, neighbour = 175, distant = 156 cells from 6 embryos; No Cre = 711 cells from 6 embryos, all imaged using AiryScan. F. Maximum-projected wholemount image showing MHC-IIb and total  $\beta$ -tubulin (Tub) staining in the mouse neuroepithelium. The cyan boxed region is shown below, with staining for tubulin but not MHC-IIb, to emphasize that cells with apical cap MHC-IIb have radial apical microtubules (e.g. cell outlined by dashed line). The bottom panel is an optical cross-section through the same embryo showing apical cap myosin (white arc) overlies cells without long tubulin tails (magenta arrows, magenta arc). G. Quantification of average tubulin tail length in No Cre and Cre;Fl/- embryos. Each point represents an individual embryo. Lengths were calculated from 3D projected images of the flat PNP neuroepithelium. A small group of tails is shown as an example and the magenta bracket indicates their length. P value from Student's T-test. H. Maximum-projected optical cross-section showing individual tubulin tails in a Cre;Fl/- embryo. White lines indicate tail length (quantified in I and G). It was not possible to reliably determine whether individual cells were apical neighbours of Vangl2-deleted cells in optical cross-sections. I. Quantification of tubulin tail lengths in Vangl2-deleted (EGFP+) and Vangl2-replete (EGFP-) neuroepithelial cells. The majority of the latter would be apical neighbours of EGFP+ cells. Optical cross-section images were saved individually and analysed blinded to EGFP expression. Points represent individual tails (EGFP = 64 tails, tdTom = 72 tails from four embryos from four independent litters). P value from Mann Whitney U-test. J. Representative surface-subtracted apical neuroepithelium of a Cre;Fl/- embryo showing apical tubulin, MHC-IIb and EGFP staining. Note: tubulin tails are not visible in surface-subtracted images. K. Quantification of tubulin staining intensity on the apical cap of surface-subtracted Vangl2-deleted (EGFP+), neighbouring (EGFP-) and distant (EGFP-) cells. Lines indicate average tubulin intensities from the same embryo, compared by repeated measures ANOVA. L. Schematic of cytoskeletal features in Vangl2-deleted (green) and neighbouring Vangl2-replete cells. Blue arrows indicate pro-constriction force generated by actomyosin (blue) and opposing force from dense apical microtubules (magenta). Vangl2-deleted cells cell-autonomously have cortical myosin associated with long tubulin tails. Their neighbours have non-cell-autonomously determined shorter tails, denser apical microtubules associated with apical cap myosin staining and less myosin along their cell-cell borders. All neuroepithelial cells are interconnected by force-transmitting adherens and tight junctions. All images were obtained using AiryScan; scale bars = 20  $\mu$ m



**Figure 6**

The proportion of Vangl2-replete cells neighbouring a deleted cell correlates with PNP eversion. A. Illustrative examples of surface-subtracted neuroepithelia with low and high levels of EGFP recombination. Cell borders were determined from Zo-1 staining. Green = Vangl2-deleted, blue = neighbour and white = distant cells. Scale bar = 50  $\mu\text{m}$ . B. Correlation between apical area and the number of neighbours (as predicted by Lewis' law) of Vangl2-deleted cells. EGFP+ cells infrequently neighbored each other so total and Vangl2-replete (tdTom) cells were counted separately. Each dot represents a cell (234 cells from three embryos). C. Positive correlation between the proportion of neuroepithelial cells which are EGFP+ and the proportion of EGFP- cells which neighbour an EGFP+ cell. Each dot represents an embryo. D. Inverse correlation between the proportion of unique Vangl2-replete neighbours per Vangl2-deleted cell and overall % Cre-mediated recombination, demonstrating that non-autonomous effect amplification is limited by neighbour-sharing. E-F. Correlation between neural fold eversion (negative elevation) in Cre;Fl- embryos and the proportion of cells which are Vangl2-deleted (E) or neighbours (F) in 15-20 somite stage embryos. The magenta box indicates the minimum degree of

neural fold elevation observed in No Cre littermates. Each dot represents an individual embryo. P values and linear trend lines from Pearson correlation.

## Supplementary Files

This is a list of supplementary files associated with this preprint. Click to download.

- [GGaleaSupplementaryFiguresandLegends.pdf](#)